JACS
JOURNAL OF THE AMERICAN CHEMICAL SOCIETY

ARTICLE

pubs.acs.org/JACS

Nanoporous Anatase TiO_2 Mesocrystals: Additive-Free Synthesis, Remarkable Crystalline-Phase Stability, and Improved Lithium Insertion Behavior

Jianfeng Ye, Wen Liu, Jinguang Cai, Shuai Chen, Xiaowei Zhao, Henghui Zhou, and Limin Qi*

Beijing National Laboratory for Molecular Sciences, State Key Laboratory for Structural Chemistry of Unstable and Stable Species, College of Chemistry, Peking University, Beijing 100871, People's Republic of China

Supporting Information

ABSTRACT: Unique spindle-shaped nanoporous anatase TiO_2 mesocrystals with a single-crystal-like structure and tunable sizes were successfully fabricated on a large scale through mesoscale assembly in the tetrabutyl titanate—acetic acid system without any additives under solvothermal conditions. A complex mesoscale assembly process involving slow release of soluble species from metastable solid precursors for the continuous formation of nascent anatase nanocrystals, oriented aggregation of tiny anatase nanocrystals, and entrapment of in situ produced butyl acetate as a porogen was put forward for the formation of the anatase mesocrystals. It was revealed that the acetic acid molecules played multiple key roles during the nonhydrolytic processing of the [001]-oriented, single-crystal-like anatase mesocrystals. The obtained nanoporous anatase mesocrystals exhibited remarkable crystalline-phase stability (i.e., the pure phase of anatase can be retained after being annealed at 900 °C) and improved performance as anode materials for lithium ion batteries, which could be largely attributed to the intrinsic single-crystal-like nature as well as high porosity of the nanoporous mesocrystals.

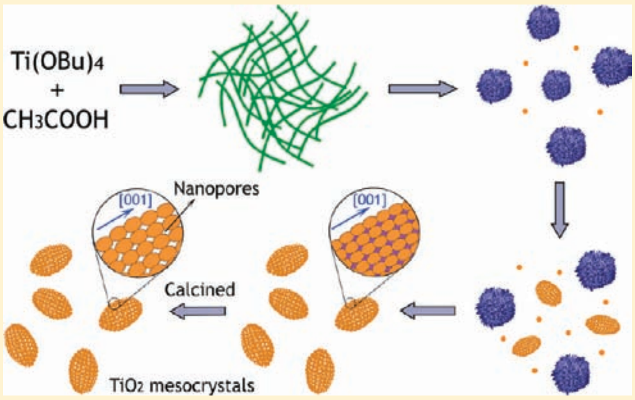

INTRODUCTION

Nanoparticles are the subject of intensive research not only because of the novel properties and functions associated with individual nanoparticles but also owing to the new collective properties and advanced tunable functions arising from nanoparticle ensembles.[1] Recently, much attention has been paid to the self-assembly and transformation of nanoparticles into highly ordered superstructures with controllable architectures.[2] Particularly, mesocrystals, which are assemblies of crystallographically oriented nanocrystals, have received rapidly increasing attention since they were first proposed as a new class of ordered nanoparticle superstructures by Cölfen and Antonietti in 2005.[3] Such mesoscopically structured crystals are conceptually different from supercrystals or nanocrystal superlattices,[1] which are periodic arrangements of nanocrystals irrespective of the mutual nanoparticle orientation. Mesocrystals are characterized by high crystallinity, high porosity, subunit alignment, and similarity to highly sophisticated biominerals, making them promising substitutes for single-crystalline or porous polycrystalline materials in many applications such as catalysis, sensing, and energy storage and conversion.[4] Despite a flourishing emergence of mesocrystals from a variety of materials including calcium carbonate,[5] organic molecules,[6] metal oxides,[7−10] and other functional materials,[11] it remains a great challenge to transfer mesocrystals into applications because their formation processes are still poorly understood and the applied organic additives are usually still too expensive for large-scale applications.[4a] Moreover, it is demanding to explore the new physical properties and chemical functions arising from the mesocrystalline superstructures of functional materials.

Titanium dioxide (TiO_2) is among the most widely investigated materials for its unique properties and many promising applications in environmental and energy areas ranging from photocatalysis and sensing to solar cells and lithium ion batteries.[12] Nanoporous TiO_2 materials with large surface areas have proved to be excellent candidates for these applications.[13,14] In general, the properties and operational performance of nanoporous TiO_2 are largely dependent on its crystal phase, crystallinity, surface area, porosity, morphology, and architecture; in this regard, TiO_2 mesocrystals with tunable architectures are promising candidates for a wide range of applications. It is noteworthy that anatase TiO_2 mesocrystals were first prepared by topotactic conversion from NH_4TiOF_3 mesocrystals, which were synthesized in the presence of nonionic surfactants.[9] Recently, there have been some efforts devoted to the direct mesoscale assembly of TiO_2 mesocrystals as well as their photocatalytic properties.[10] In these mesoscale transformation processes, solid templates[10a] and organic additives[10b,c] were generally employed, whereas the only additive-free synthesis resulted in the formation of rutile TiO_2 mesocrystals with a low surface area (16 $m^2\ g^{-1}$), which

Received: September 11, 2010
Published: December 10, 2010

dx.doi.org/10.1021/ja108205q | *J. Am. Chem. Soc.* 2011, 133, 933–940

were spherical aggregates of radially aligned rutile nanowires.[10d] Therefore, it is highly desirable to explore the additive-free approaches toward TiO_2 mesocrystals with high crystallinity and high porosity.

Herein, we report on the first additive-free synthesis of nanoporous anatase TiO_2 mesocrystals with a single-crystal-like structure by using tetrabutyl titanate as the titanium source and acetic acid as the solvent. A complex mesoscale assembly process involving slow release of soluble species from metastable solid precursors for the continuous formation of nascent anatase nanocrystals, oriented aggregation of tiny anatase nanocrystals, and entrapment of in situ produced butyl acetate as a porogen is proposed for the formation of the unique, spindle-shaped, anatase mesocrystals. Moreover, remarkable crystalline-phase stability and improved performance as anode materials for lithium ion batteries are demonstrated for the obtained nanoporous anatase mesocrystals.

EXPERIMENTAL SECTION

Materials and Synthesis. Acetic acid (HAc) and tetrabutyl titanate (TBT) were purchased from Beijing Chemical Reagent Co. and Beijing Great Wall Chemical Reagent Co., respectively, and used without further purification. The fabrication of nanoporous anatase TiO_2 mesocrystals was simply achieved by the solvothermal reaction of the TBT—HAc solution. In a typical synthesis, 0.2 mL of TBT was added dropwise to 10 mL of HAc with continuous stirring. The obtained white suspension was transferred to a 20 mL Teflon-lined stainless-steel autoclave, which was then heated at 200 °C for 24 h. After the autoclave cooled to room temperature, the product was collected by centrifugation, washed with ethanol several times, dried at 60 °C overnight, and calcined at 400 °C for 30 min to remove the residual organics.

Characterization. The obtained products were characterized by scanning electron microscopy (SEM, Hitachi S4800, 5 kV), transmission electron microscopy (TEM, JEOL JEM 200CX, 160 kV), high-resolution TEM (HRTEM, FEI Tecnai F30, 300 kV), powder X-ray diffraction (XRD, Rigaku Dmax-2000, Cu Kα), and Fourier transform IR spectroscopy (FTIR, Nicolet Magna-IR 750). Thermogravimetric analysis (TGA) was carried out on a Q600 SDT thermoanalyzer (Thermal Analysis) with air as the carrier gas at a heating rate of 10 °C min^{-1}. Nitrogen adsorption—desorption measurements were performed using a Micromeritics ASAP 2010 instrument. The pore size distribution was calculated from the adsorption branch of the sorption isotherms using the Barret—Joyner—Halenda (BJH) method. Gas chromatography/mass spectroscopy (GC/MS) analysis was conducted on a 7890A/5975B GC/MS system with helium as the carrier gas.

Electrochemical Measurement. Electrochemical charge and discharge tests were made in 2032 coin cells. The anode mixture was prepared by mixing the active materials, acetylene black, and binder polytetrafluoroethylene (PTFE) at a ratio of 84:10:6. The mixture was then rolled into a 0.2-mm-thick sheet and punched into disks with a diameter of 7 mm. A typical electrode sheet contained about 6 mg of active material. Prior to use, the electrode sheet was dried under vacuum at 120 °C overnight. The electrode was assembled in an argon-filled glovebox. Li foil was used as the counter electrode, 1 M $LiClO_4$ in propylene carbonate (PC) and dimethyl carbonate (1:1 by volume) was used as the electrolyte, and Celgard 2400 was used as the separator. The electrochemical performances were evaluated by using a LAND CT2001A battery test system. All electrochemical experiments were operated at room temperature (25 °C). The coin cells were discharged and charged between 3.0 and 1.0 V at a constant current (1 C rate taken to be 170 mA g^{-1}). Cyclic voltammetry was carried out using a three-electrode system. A platinum powder microelectrode containing 84% active material, 10% acetylene black, and 6% PTFE was applied as working electrode and Li metal foil as both the counter electrode and reference electrode. The electrochemical response was measured on a CHI660C electrochemical workstation in the voltage range of 3.0—1.0 V (versus Li/Li^+) at a sweep rate of 0.1 mV s^{-1}.

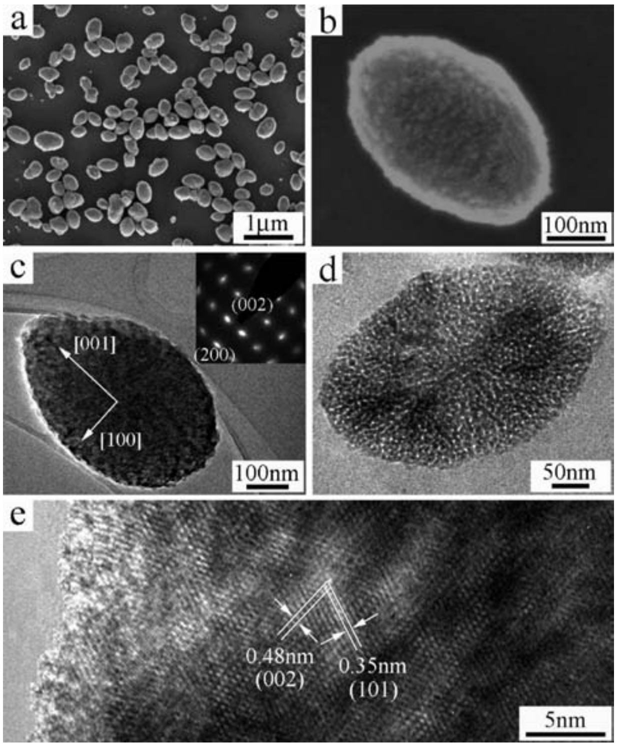

Figure 1. SEM (a,b), TEM (c,d), and HRTEM (e) images of nanoporous anatase TiO_2 mesocrystals. The inset in (c) shows the SAED pattern related to the whole particle, and plate (d) was obtained from a microtomed sample.

RESULTS AND DISCUSSION

The synthesis of nanoporous anatase TiO_2 mesocrystals was simply achieved by the solvothermal treatment of the solution of TBT in HAc and subsequent calcination at 400 °C. Figure 1a shows a low-magnification SEM image of the product obtained after solvothermal reaction at 200 °C for 24 h and subsequent calcination at 400 °C for 30 min to remove the residual organics, which suggests the large-scale formation of submicrometer-sized, spindle-shaped particles predominantly 300—450 nm in length (~380 nm on average) and 200—350 nm in diameter (~280 nm on average). It may be noted that a small amount of twinned particles coexist with the isolated individual particles with a proportion ~10% throughout the whole product. The related XRD pattern shown in Figure 2a exhibits broadened diffraction peaks exclusively ascribed to TiO_2 crystals with the tetragonal anatase phase (JCPDS No. 21-1272). Detailed analysis of the peak broadening of the (101) reflection using the Scherrer equation indicates an average crystallite size ~14 nm, suggesting that these anatase TiO_2 particles are composed of nanocrystal subunits. A high-magnification SEM image shown in Figure 1b reveals that the particle surface is relatively rough and apparently built from tiny nanoparticles with diameters around 10—20 nm, which is consistent with the XRD result. Figure 1c shows a typical TEM image of a single particle, confirming that the particle consists of nanosized subunits. The related selected area electron diffraction (SAED) pattern exhibits diffraction spots corresponding

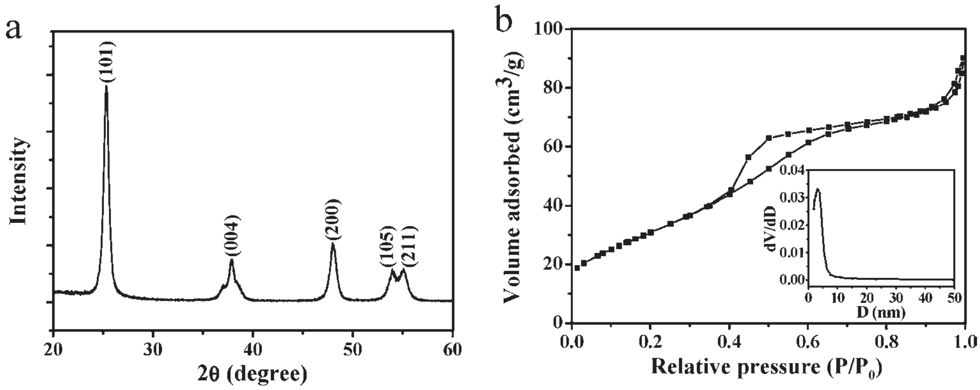

Figure 2. XRD pattern (a) and N_2 adsorption−desorption isotherms (b) of nanoporous anatase TiO_2 mesocrystals. Inset shows the pore size distribution obtained from the adsorption branch.

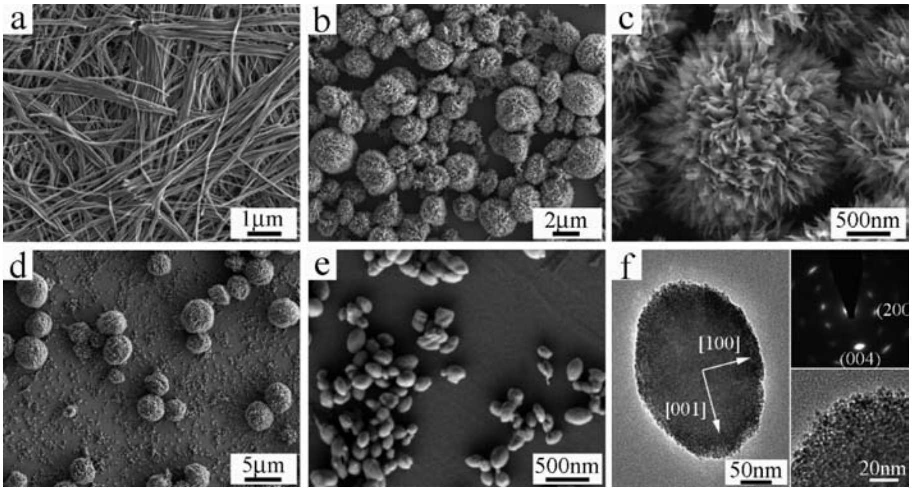

Figure 3. SEM (a−e) and TEM (f) images of the precipitates obtained at different reaction times: (a) 1, (b,c) 2, and (d−f) 5 h. The upper right inset in (f) shows the related SAED pattern, and the lower right inset is an enlarged TEM image.

to the [010] zone axis of the anatase phase, indicating that the whole particle has a "single-crystal-like" structure. It suggests that the whole assembly of the nanoparticle subunits is highly oriented, leading to the formation of the spindle-like particle elongated along the [001] direction. The diffraction spots are slightly elongated, indicating that there is small lattice mismatch between the boundaries of the nanoparticles when they are assembled in the same orientation, typical for mesocrystals.[3,4] The internal porosity of the particle is revealed by the TEM image taken on a microtomed sample (Figure 1d), which preliminarily shows the existence of evenly distributed nanopores inside the particle, supporting the formation of nanoporous mesocrystals. This result was confirmed by the corresponding nitrogen adsorption/desorption measurement, which indicated the presence of rather uniform nanopores with an average diameter of 3.9 nm (Figure 2b). The Brunauer−Emmett−Teller (BET) surface area and the pore volume were determined to be 114 $m^2\ g^{-1}$ and 0.14 $m^3\ g^{-1}$, respectively. Figure 1e shows an HRTEM image of the particle shown in Figure 1c, further confirming its single-crystal-like nature. The clear lattice fringes can be well assigned to the (101) and (002) spacings of anatase, while atomic defects and planar mismatches in or among the crystallites are visible, in good agreement with the SAED pattern. A careful HRTEM observation of the end of the spindle-shaped particle suggests that some [001]-oriented, elongated subunits (about 10−18 nm in width) protruded, which were parallel to the long axis of the [001]-oriented, spindle-shape particle (Figure S1, Supporting Information). It can be seen that elongated subunits frequently exposed the side facets of the {101} planes together with the end facet of the {001} planes, which were reminiscent of the truncated bipyramid anatase seeds with two end (001) facets and eight equivalent side {101} facets that underwent one-dimensional oriented attachment along the [001] direction through elimination of the {001} facets with a relatively higher surface energy.[15] Considering the small crystallite size of primary building units revealed by the XRD pattern and the presence of internal nanopores indicated by the N_2 sorption measurement, as well as the electron microscopy characterizations, it can be concluded that nanoporous, single-crystal-like, spindle-shaped, anatase TiO_2 mesocrystals with high crystallinity and high porosity were successfully fabricated on a large scale in the solution of TBT in acetic acid without any additives.

To shed light on the formation mechanism of these nanoporous anatase TiO_2 mesocrystals, their growth process was followed by examining the products harvested at different intervals of reaction time. The precipitates obtained at different reaction times without calcination were characterized by electron microscopy (Figure 3), XRD (Figure S2, Supporting Information), and

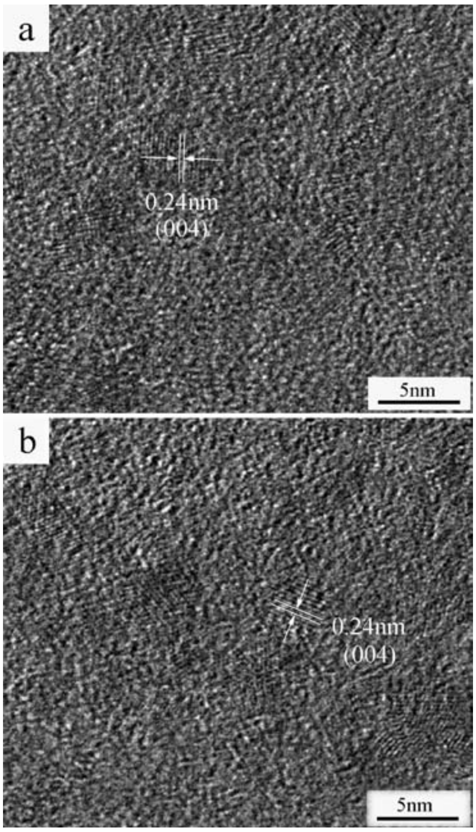

Figure 4. HRTEM images of anatase nanocrystals harvested at different reaction times: (a) 2 and (b) 5 h. The samples were prepared from the supernatant solutions after removing the precipitate by centrifugation at 4000 rpm.

FTIR (Figure S3, Supporting Information). As shown in Figure 3a, nanofiber bundles with an interlaced structure were the dominant product after 1 h of reaction. No obvious diffraction peaks are observed in the XRD pattern, suggesting that the nanofiber precursor adopts an amorphous phase. The emergence of the asymmetric and symmetric stretching vibrations of the carboxylic group centered at 1540, 1452, and 1421 cm^{-1} in the FTIR spectra reveals the coordination of HAc to titanium centers,[16a,b] indicating the formation of a titanium-containing precursor (hereafter denoted as precursor A). The frequency separation ($\Delta\nu$ = 119 cm^{-1}) between 1540 and 1421 cm^{-1} suggests that acetate acts preferentially as a bidentate rather than a bridging ligand between two titanium atoms.[10c] When the reaction time was increased to 2 h, all the nanofiber bundles disappeared and flower-like particles about 2−5 μm in diameter, which were assembled from leaf-like nanosheets, were produced (Figure 3b,c). The XRD pattern suggests that the flower-like precursor adopts an unknown crystalline phase. In the FTIR spectrum, two sharp bands at 1721 and 1259 cm^{-1} appeared, which could be attributed to the monodentate-coordinated acetates,[16c] indicating the formation of another kind of titanium-containing precursor (hereafter denoted as precursor B). It is noteworthy that, at this stage, many tiny anatase TiO_2 nanocrystals about 3−5 nm in diameter coexisted with the micrometer-sized flower-like particles in the reaction solution (Figure 4a).

When the reaction time was further increased to 5 h, many smaller ellipsoidal particles appeared in addition to the residual flower-like particles (Figure 3d). An enlarged SEM image shown in Figure 3e suggests that these submicrometer-sized particles were basically spindle-shaped, with lengths 200−350 nm (~280 nm on average) and diameters in the range of 120−220 nm (~160 nm on average). Typical TEM images of a single spindle-shaped particle are shown in Figure 3f, which reveal that the obtained particles were assembled from nanocrystal subunits about 3−5 nm in diameter. The related SAED pattern suggests that the particle actually adopted a single-crystal-like mesoscopic structure elongated along the [001] direction. Interestingly, the size of the nanocrystal subunits was nearly identical to that of the anatase nanocrystals dispersed in the solution (Figure 4b), indicating the oriented aggregation of tiny anatase nanocrystals into ordered superstructures. Upon the gradual dissolving of the flower-like particles, pure spindle-shaped, anatase TiO_2 mesocrystals with a larger subunit size (~10 nm), which was estimated from the peak width analysis of the (101) reflection of the related XRD pattern according to the Scherrer equation, were produced when the reaction time was prolonged to 24 h (Figure S4, Supporting Information). Such a formation process of anatase mesocrystals accompanied by the gradual decomposition of the titanium-containing precursor B was supported by the related XRD patterns and FTIR spectra (Figures S2 and S3, Supporting Information). It is worth noting that, after 24 h of reaction, the XRD pattern exhibits only diffraction peaks attributed to anatase crystals, whereas the FTIR spectrum shows the presence of absorption bands centered at 1526 and 1421 cm^{-1}, attributed to the chelating acetate ligands in addition to the broad and strong absorption around 600 cm^{-1} assigned to the Ti−O−Ti moiety of anatase TiO_2. This result indicates that butyl acetate could be produced from the reaction between $Ti(OC_4H_9)_4$ and acetic acid, which were then entrapped inside the assembled anatase mesocrystals and acted as a porogen for the formation of the final nanoporous anatase mesocrystals after calcination. Actually, an intense odor of ester was noticed from the solution after the reaction, and further FTIR analysis conducted on the supernatant solutions after removing the precipitate showed an enhanced absorption of the 1250 cm^{-1} band (C−O stretching of butyl acetate) compared with acetic acid (Figure S5, Supporting Information). Furthermore, GC/MS analysis conducted on the extract of the final reaction solution clearly revealed the existence of butyl acetate (Figure S6, Supporting Information), confirming the formation of butyl acetate during the synthetic procedure. Moreover, TGA indicated that a considerable amount of butyl acetate (~6.3 wt %) was entrapped inside the TiO_2 mesocrystals, and the complete decomposition of organics occurred around 400 °C (Figure S7, Supporting Information). Finally, calcination at 400 °C for 30 min resulted in the formation of pure nanoporous anatase TiO_2 mesocrystals shown in Figure 1, which was accompanied by a further increase in the average size of nanocrystal subunits from ~10 to ~14 nm, owing to the further growth of nanocrystals during thermal treatment.

Accordingly, a tentative mechanism for the formation of anatase TiO_2 mesocrystals was proposed as illustrated in Scheme 1. In the current solvothermal synthesis at 200 °C, the reaction between $Ti(OC_4H_9)_4$ and HAc first resulted in the coordination of HAc to titanium centers to form unstable titanium acetate complexes $(CH_3COO)_xTi(OC_4H_9)_{4-x}$ by ligand exchange/substitution, concomitant with the release of C_4H_9OH (eq 1). The produced C_4H_9OH could then react with the solvent HAc to form water by a slow esterification reaction (eq 2). Subsequently, Ti−O−Ti bonds would form by both hydrolysis−condensation

Scheme 1. Schematic Illustration of a Tentative Mechanism for the Formation of Nanoporous Anatase TiO_2 Mesocrystals without Additives

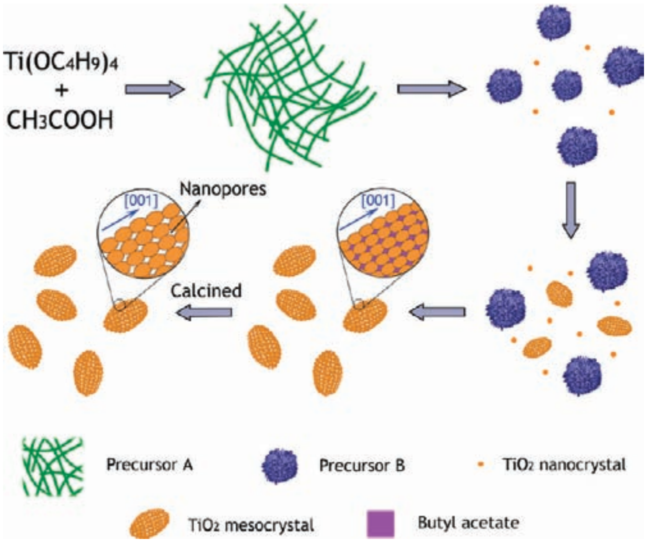

and nonhydrolytic condensation processes (eqs 3 and 4),[16b] leading to the formation of the transient amorphous fiber-like precursor A.

$$Ti(OC_4H_9)_4 + xCH_3COOH \rightarrow (CH_3COO)_xTi(OC_4H_9)_{4-x} + xC_4H_9OH \qquad (1)$$

$$C_4H_9OH + CH_3COOH \rightarrow CH_3COOC_4H_9 + H_2O \qquad (2)$$

$$\equiv Ti{-}OR + H_2O \rightarrow \equiv Ti{-}OH + ROH \quad (R = C_4H_9 \text{ or } CH_3CO) \qquad (3)$$

$$\equiv Ti{-}OR' + \equiv Ti{-}OR'' \rightarrow \equiv Ti{-}O{-}Ti\equiv + R'OR'' \quad (R' = H \text{ or } CH_3CO;\ R'' = H \text{ or } C_4H_9) \qquad (4)$$

The formation of the amorphous precursor in the form of nanofibers is surprising, and the exact reason remains unknown. A possible explanation might be that linear condensation occurred preferentially under the current conditions, leading to the formation of the amorphous nanofibers. With the two condensation processes continuing, the crystallized flower-like precursor B emerged at the expense of the transient precursor A. The metastable precursor B would then act as a reservoir to gradually release soluble titanium-containing species for the nucleation and growth of anatase nanocrystals in the solution. These tiny anatase nanocrystals (3−5 nm in diameter) underwent oriented aggregation along the [001] direction, together with some lateral attachment along some side facets such as the {101} facets, accompanied by the entrapment of in situ produced butyl acetate, resulting in the formation of the spindle-shaped, anatase mesocrystals elongated along the [001] direction. It is known that massive precipitation of amorphous TiO_2 inevitably occurs in most sol−gel preparations due to the very fast hydrolysis and condensation rate and hence the uncontrolled branching of the resulting Ti−O−Ti network. To exhibit control over the evolution of the oxide structure and morphology, carboxylic acids can be employed both as stabilizing solvent and as chemical modifier of titanium alkoxides to lower the reactivity of the precursors.[16a,16b,17] In the current situation, the nascent anatase nanocrystals with high surface energies might be temporarily stabilized by acetic acid, which could then orient each other to form a crystallographic oriented mesocrystalline architecture with some butyl acetate enwrapped in the interparticle pores. Finally, nanoporous anatase TiO_2 mesocrystals with preserved morphology will result from removal of the organic residuals by subsequent calcination, accompanied by a moderate increase in the size of the nanocrystal subunits.

It has been documented that nonhydrolytic (or nonaqueous) sol−gel routes for nanocrystalline metal oxides constitute one of the most versatile and powerful synthesis methodologies with a high control over composition, morphology, and structure.[18] However, acetic acid has been rarely used as the sole solvent for the nonhydrolytic synthesis of metal oxides.[16b] During the mesoscale assembly of the current spindle-shaped, anatase mesocrystals with a single-crystal-like structure, the solvent acetic acid played multiple roles. First, it acted as the chemical modifier of TBT to lower its reactivity. Second, it reacted with TBT to form transient or metastable precursors for slow release of soluble titanium-containing species for the continuous formation of nascent anatase nanocrystals. Third, it acted as the stabilizing solvent to temporarily stabilize the tiny anatase nanocrystals against immediate single crystal formation or uncontrolled aggregation, but the binding to the {001} facets was relative weak, so that the subsequent oriented attachment along the [001] direction could take place readily. Fourth, it reacted with TBT to produce butyl acetate that played the role of porogen or template during the oriented aggregation of anatase nanocrystals to form mesocrystals. It is expected that adding additional water into the TBT−HAc system will greatly accelerate the hydrolysis−condensation process and weaken the stabilizing effect of acetic acid. It was found that spindle-shaped, anatase mesocrystals with smaller sizes (about 80−120 nm in length) but a larger subunit size (~12 nm) were obtained when 0.1 mL of water was added into the TBT−HAc solution (~10 mL), whereas only anatase nanocrystals about 14 nm in size were obtained due to the very fast hydrolysis−condensation process when the amount of water added was increased to 1 mL (Figure 5). This result may be rationalized by considering that the effect of HAc could be gradually impaired with increasing water content, until finally mesocrystals could not be assembled from the relatively large nanocrystals.

It is expected that the size of the mesocrystals may be controlled via simply adjusting the concentration of the preformed nascent TiO_2 nanocrystals since the mesocrystals formed through oriented aggregation of these nanocrystal subunits. Actually, spindle-shaped, anatase mesocrystals about 200−350 nm in length (Figure 6a) were obtained when 0.35 mL of TBT was added into 10 mL of HAc, considerably smaller than the mesocrystals obtained with 0.2 mL of TBT (300−450 nm in length, as shown in Figure 1). Similarly, the obtained spindle-shaped, anatase mesocrystals exhibited a single-crystal-like structure with the length axis along the [001] direction (Figure 6b). If the amount of TBT added was further increased to 0.5 mL, [001]-oriented, single-crystal-like anatase mesocrystals with even smaller dimensions (about 100−150 nm in length) emerged (Figure 6c,d). These results suggest that [001]-oriented, single-crystal-like anatase mesocrystals with tunable sizes can be readily

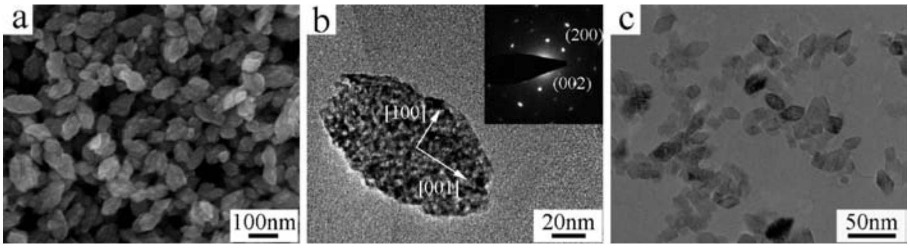

Figure 5. SEM (a) and TEM (b,c) images of the anatase products obtained with different amounts of added water: (a,b) 0.1 and (c) 1 mL. Inset shows the related SAED pattern.

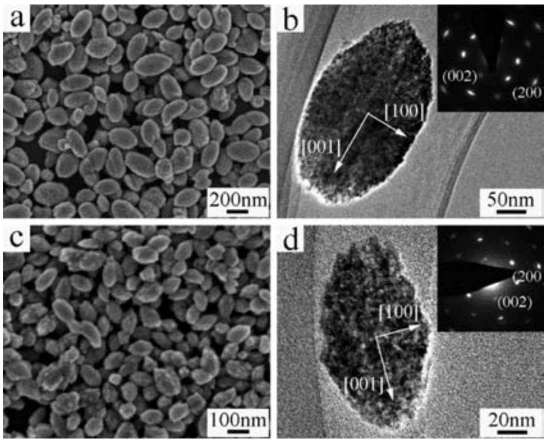

Figure 6. SEM (a,c) and TEM (b,d) images of the as-precipitated anatase mesocrystals obtained with different amounts of TBT: (a,b) 0.35 and (c,d) 0.5 mL. Insets show the related SAED patterns.

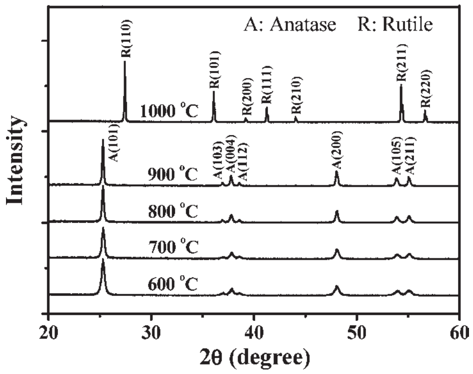

Figure 7. XRD patterns of nanoporous anatase TiO_2 mesocrystals calcined at different temperatures.

prepared by changing the TBT concentration in the TBT−HAc system.

The anatase-to-rutile phase transformation in TiO_2 has attracted much attention since the phase structure of titania nanostructures largely determines their suitability for practical applications.[19,20] It has been documented that the transformation usually occurs at a temperature range of 500−700 °C under normal conditions, and many attempts including doping and surface modification have been made to inhibit the phase transformation of anatase.[19] Herein, the phase stability of the obtained nanoporous anatase mesocrystals was investigated by examining the XRD patterns of the mesocrystals annealed at different temperatures, as shown in Figure 7. It can be seen that the anatase mesocrystals showed extremely high crystalline-phase stability, retaining the pure phase of anatase even after being calcined at 900 °C. In contrast, the phase transformation of the anatase nanocrystals (∼15 nm in size), which were obtained by addition of 1 mL of water into the TBT−HAc system and calcination at 400 °C, started at 800 °C, and the rutile phase existed as the predominant crystal phase at 900 °C (Figures S8 and S9, Supporting Information). It has been demonstrated that the phase transformation of agglomerated TiO_2 nanoparticles starts from the interfaces of contacting anatase grains, which provide the nucleation sites of the rutile phase.[20] In the current situation, the interfacial nucleation sites were largely eliminated since the crystallographically oriented nanocrystals were connected by mineral necks in the single-crystal-like anatase mesocrystals, leading to a remarkably enhanced phase stability. It may be noted that, after calcination at 900 °C, the nanoporous anatase mesocrystals were converted into solid single crystals of anatase due to the sintering of the nanocrystal subunits (Figure S10, Supporting Information), indicating that nanoporous mesocrystals may eventually fuse into nonporous single crystals under suitable annealing conditions.

There is much recent interest in TiO_2 nanostructures due to their potential advantages (e.g., safety, rate) as anode materials in a new generation of lithium ion batteries.[12d,14] Therefore, the properties of the nanoporous anatase mesocrystals as a lithium insertion host were investigated. Figure 8a shows the cyclic voltammograms (CV) of the obtained nanoporous anatase mesocrystals at a scan rate of 0.1 mV s^{-1} in the potential range from 3.0 to 1.0 V. The clear cathodic/anodic peaks located at 1.68 and 2.06 V (versus Li^+/Li) are associated with lithium insertion/extraction in the anatase lattice, which is consistent with the previous report.[21] Figure 8b presents the rate capability of the nanoporous TiO_2 mesocrystals assembled from anatase nanocrystals (∼14 nm in size) together with the anatase nanocrystals (∼15 nm in size) from 0.05 to 2 C (1 C = 170 mA g^{-1}) for five cycles at each current rate. It is revealed that the mesocrystal electrode retained good rate capability as the current density increased by 40 times. At low current rates, the capacities of the mesocrystals and nanocrystals are comparable; however, the difference increased considerably as the current rate was increased. We propose that the facile electronic conduction and fast Li ion transport between the electrolyte and the mesocryatal electrode, where crystallographically oriented anatase nanocrystals were well connected with few grain boundaries, largely contributed to the improved lithium insertion behavior compared with the nanocrystal electrode, where irregularly oriented anatase nanocrystals were connected with many grain boundaries. Moreover, the uniform nanopores in the anatase mesocrystals could facilitate their contact with electrolyte and hence maximize the electrode/electrolyte contact area, favoring fast Li ion transport, whereas the porosity between the nanocrystals is random in size, with some voids being too small for electrolyte

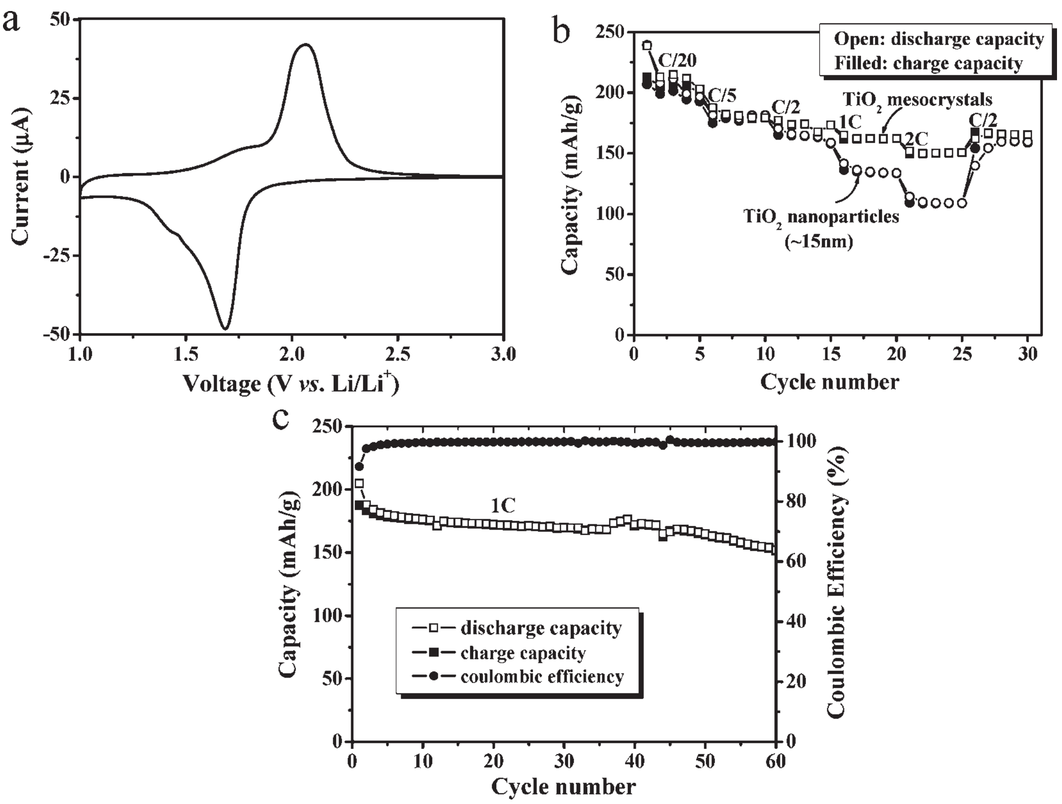

Figure 8. (a) Cyclic voltammograms of nanoporous anatase TiO_2 mesocrystals between 3.0 and 1.0 V with a scan rate of 0.1 mV s^{-1}. (b) Rate capability of nanoporous mesocrystals and nanocrystals of anatase TiO_2 from C/20 to 2 C (1 C = 170 mA/g) for five cycles. (c) Cycling performance of nanoporous anatase TiO_2 mesocrystals with a current rate of 1 C.

ingress and some too large.[14a] It is notable that the anatase mesocrystals were able to deliver specific discharge capacities of 164.9 and 151.7 mAh g^{-1} at 1 and 2 C, respectively, indicating a performance higher than that of anatase hollow spheres[22a] and comparable with that of mesoporous spheres composed of tiny anatase nanocrystals.[22b] The anatase mesocrystal electrode also demonstrated nice cyclability. As shown in Figure 8c, the mesocrystals showed a discharge capacity of 204.7 mAh g^{-1} in the first cycle and a high first cycle efficiency of 91.6% at a current density of 1 C. Good capacity retention was realized over extended cycling: approximately 74.2% (151.9 mAh g^{-1}) of its initial discharge capacity was retained after 60 cycles. The average capacity fading per cycle was close to 0.5%, and Coulombic efficiency was nearly 100% at each cycle. The improved lithium insertion behavior of the nanoporous anatase mesocrystals makes them a promising candidate for application as an anode material in lithium batteries. Compared with graphite, a current technical standard material for lithium ion battery anodes with a theoretical capacity of 372 mAh g^{-1}, the current mesocrystal TiO_2 anode material still has a lower capacity, but it has considerable advantages in terms of safety and rate.[12e] It may be reasonably expected that the lithium storage performance of the nanoporous anatase mesocrystals could be further improved if the optimization of the pore structure of the mesocrystalline architectures is achieved.

■ CONCLUSIONS

In conclusion, unique spindle-shaped, nanoporous, anatase TiO_2 mesocrystals with a single-crystal-like structure and tunable sizes were successfully fabricated on a large scale through mesoscale assembly in the TBT−HAc system without any additives under solvothermal conditions. A complex mesoscale assembly process involving slow release of soluble species from metastable solid precursors for the continuous formation of nascent anatase nanocrystals, oriented aggregation of tiny anatase nanocrystals, and entrapment of in situ produced butyl acetate as a porogen was put forward for the formation of the anatase mesocrystals. It was revealed that the HAc molecules played multiple roles during the nonhydrolytic processing of anatase mesocrystals in the binary TBT−HAc system. It was demonstrated that the obtained nanoporous anatase mesocrystals exhibited remarkable crystalline-phase stability and improved performance as anode materials for lithium ion batteries, which could be largely attributed to the intrinsic single-crystal-like nature as well as the high porosity of the nanoporous mesocrystals. This result may shed light on the mesoscale assembly mechanism of mesocrystals from synthetic materials and open a new avenue for large-scale synthesis of nanoporous mesocrystals of functional materials with high crystallinity, high porosity, and promising applications in energy and environmental fields.

■ ASSOCIATED CONTENT

Ⓢ Supporting Information. Additional XRD, FTIR, TGA, SEM, and TEM characterization of the TiO_2 products obtained at different conditions, and GC/MS analysis of the final reaction solution. This material is available free of charge via the Internet at http://pubs.acs.org.

AUTHOR INFORMATION

Corresponding Author
liminqi@pku.edu.cn

ACKNOWLEDGMENT

Financial support from NSFC (Grants 20873002, 21073005, 20633010, and 50821061) and MOST (Grant 2007CB936201) is gratefully acknowledged.

REFERENCES

(1) (a) Talapin, D. V.; Lee, J.-S.; Kovalenko, M. V.; Shevchenko, E. V. *Chem. Rev.* **2010**, *110*, 389. (b) Goesmann, H.; Feldmann, C. *Angew. Chem., Int. Ed.* **2010**, *49*, 1362.

(2) (a) Mann, S. *Nat. Mater.* **2009**, *8*, 781. (b) Nie, Z.; Petukhova, A.; Kumacheva, E. *Nat. Nanotech.* **2010**, *5*, 15. (c) Grelczak, M.; Vermant, J.; Furst, E. M.; Liz-Marzán, L. M. *ACS Nano* **2010**, *4*, 3591. (d) Srivastava, S.; Kotov, N. A. *Soft Matter* **2009**, *5*, 1146. (e) Srivastava, S.; Santos, A.; Critchley, K.; Kim, K.-S.; Podsiadlo, P.; Sun, K.; Lee, J.; Xu, C.; Lilly, G. D.; Glotzer, S. C.; Kotov, N. A. *Science* **2010**, *327*, 1355. (f) Dong, A.; Chen, J.; Vora, P. M.; Kikkawa, J. M.; Murray, C. B. *Nature* **2010**, *466*, 474. (g) Bierman, M. J.; Lau, Y. K. A.; Kvit, A. V.; Schmitt, A. L.; Jin, S. *Science* **2008**, *320*, 1060.

(3) (a) Cölfen, H.; Antonietti, M. *Angew. Chem., Int. Ed.* **2005**, *44*, 5576.(b) Cölfen, H.; Antonietti, M. *Mesocrystals and Nonclassical Crystallization*; John Wiley & Sons: Chichester, U.K., 2008.

(4) (a) Song, R.-Q.; Cölfen, H. *Adv. Mater.* **2010**, *22*, 1301. (b) Zhou, L.; O'Brien, P. *Small* **2008**, *4*, 1566.

(5) (a) Wang, T.; Cölfen, H.; Antonietti, M. *J. Am. Chem. Soc.* **2005**, *127*, 3246. (b) Wang, T.; Antonietti, M.; Cölfen, H. *Chem. Eur. J.* **2006**, *12*, 5722. (c) Xu, A.-W.; Antonietti, M.; Cölfen, H.; Fang, Y.-P. *Adv. Funct. Mater.* **2006**, *16*, 903. (d) Kulak, A. N.; Iddon, P.; Li, Y.; Armes, S. P.; Cölfen, H.; Paris, O.; Wilson, R. M.; Meldrum, F. C. *J. Am. Chem. Soc.* **2007**, *129*, 3729. (e) Li, W.; Wu, P. *CrystEngComm* **2009**, *11*, 2466. (f) You, C.; Zhang, Q.; Jiao, Q.; Fu, Z. *Cryst. Growth Des.* **2009**, *9*, 4720. (g) Zhu, Y.; Liu, Y.; Ruan, Q.; Zeng, Y.; Xiao, J.; Liu, Z.; Cheng, L.; Xu, F.; Zhang, L. *J. Phys. Chem. C* **2009**, *113*, 6584. (h) Kumar, S.; Ito, T.; Yanagihara, Y.; Oaki, Y.; Nishimura, T.; Kato, T. *CrystEngComm* **2010**, *12*, 2021. (i) Geng, X.; Liu, L.; Jiang, J.; Yu, S.-H. *Cryst. Growth Des.* **2010**, *10*, 3448.

(6) (a) Wohlrab, S.; Pinna, N.; Antonietti, M.; Cölfen, H. *Chem. Eur. J.* **2005**, *11*, 2903. (b) Ma, Y.; Cölfen, H.; Antonietti, M. *J. Phys. Chem. B* **2006**, *110*, 10822. (c) Medina, D. D.; Mastai, Y. *Cryst. Growth Des.* **2008**, *8*, 3646. (d) Lee, T.; Zhang, C. W. *Pharm. Res.* **2008**, *25*, 1563. (e) Huang, M.; Schilde, U.; Kumke, M.; Antonietti, M.; Cölfen, H. *J. Am. Chem. Soc.* **2010**, *132*, 3700.

(7) (a) Peng, Y.; Xu, A. W.; Deng, B.; Antonietti, M.; Cölfen, H. *J. Phys. Chem. B* **2006**, *110*, 2988. (b) Mo, M. S.; Lim, S. H.; Mai, Y. W.; Zheng, R. K.; Ringer, S. P. *Adv. Mater.* **2008**, *20*, 339. (c) Li, Z. H.; Gessner, A.; Richters, J. P.; Kalden, J.; Voss, T.; Kubel, C.; Taubert, A. *Adv. Mater.* **2008**, *20*, 1279. (d) Li, Z.; Shkilnyy, A.; Taubert, A. *Cryst. Growth Des.* **2008**, *8*, 4526. (e) Liu, Z.; Wen, X. D.; Wu, X. L.; Gao, Y. J.; Chen, H. T.; Zhu, J.; Chu, P. K. *J. Am. Chem. Soc.* **2009**, *131*, 9405. (f) Tseng, Y.-H.; Lin, H.-Y.; Liu, M.-H.; Chen, Y.-F.; Mou, C.-Y. *J. Phys. Chem. C* **2009**, *113*, 18053. (g) Ye, F.; Peng, Y.; Chen, G.-Y.; Deng, B.; Xu, A.-W. *J. Phys. Chem. C* **2009**, *113*, 10407.

(8) (a) Polleux, J.; Pinna, N.; Antonietti, M.; Niederberger, M. *J. Am. Chem. Soc.* **2005**, *127*, 15595. (b) Ge, J. P.; Hu, Y. X.; Biasini, M.; Beyermann, W. P.; Yin, Y. D. *Angew. Chem., Int. Ed.* **2007**, *46*, 4342. (c) Fang, X.-L.; Chen, C.; Jin, M.-S.; Kuang, Q.; Xie, Z.-X.; Xie, S.-Y.; Huang, R.-B.; Zheng, L.-S. *J. Mater. Chem.* **2009**, *19*, 6154. (d) Liang, X.; Gao, L.; Yang, S.; Sun, J. *Adv. Mater.* **2009**, *21*, 2068.

(9) (a) Zhou, L.; Boyle, D. S.; O'Brien, P. *Chem. Commun.* **2007**, 144. (b) Zhou, L.; Boyle, D. S.; O'Brien, P. *J. Am. Chem. Soc.* **2008**, *130*, 1309.

(10) (a) Liu, B.; Zeng, H. C. *Chem. Mater.* **2008**, *20*, 2711. (b) Liu, S.-J.; Gong, J.-Y.; Hu, B.; Yu, S.-H. *Cryst. Growth. Des.* **2009**, *9*, 203. (c) Li, L.; Liu, C. *CrystEngComm* **2010**, *12*, 2073. (d) Zhang, D.; Li, G.; Wang, F.; Yu, J. C. *CrystEngComm* **2010**, *12*, 1759.

(11) (a) Yuwono, V. M.; Burrows, N. D.; Soltis, J. A.; Penn, R. L. *J. Am. Chem. Soc.* **2010**, *132*, 2163. (b) Buscaglia, M. T.; Buscaglia, V.; Bottino, C.; Viviani, M.; Fournier, R.; Sennour, M.; Presto, S.; Marazza, R.; Nanni, P. *Cryst. Growth Des.* **2008**, *8*, 3847. (c) Bilecka, I.; Hintennach, A.; Djerdj, I.; Novák, P.; Niederberger, M. *J. Mater. Chem.* **2009**, *19*, 5125. (d) Uchiyama, H.; Imai, H. *Cryst. Growth Des.* **2010**, *10*, 1777. (e) Hu, B.; Wu, L.-H.; Liu, S.-J.; Yao, H.-B.; Shi, H.-Y.; Li, G.-P.; Yu, S.-H. *Chem. Commun.* **2010**, *46*, 2277. (f) Zhou, L.; Wang, W.; Xu, H. *Cryst. Growth Des.* **2008**, *8*, 728. (g) Hu, M.; Jiang, J.-S.; Jia, R.-P.; Zeng, Y. *CrystEngComm* **2009**, *11*, 2257. (h) Fang, J.; Ding, B.; Song, X. *Cryst. Growth Des.* **2008**, *8*, 3616. (i) Fang, J.; Ding, B.; Song, X.; Han, Y. *Appl. Phys. Lett.* **2008**, *92*, 173120.

(12) (a) Chen, X.; Mao, S. S. *Chem. Rev.* **2007**, *107*, 2891. (b) Fujishima, A.; Zhang, X.; Tryk, D. A. *Surf. Sci. Rep.* **2008**, *63*, 515. (c) Grätzel, M. *Nature* **2001**, *414*, 338. (d) Grätzel, M. *J. Photochem. Photobiol. C* **2003**, *4*, 145. (e) Deng, D.; Kim, M. G.; Lee, J. Y.; Cho, J. *Energy Environ. Sci.* **2009**, *2*, 818.

(13) (a) Kim, D.; Lee, K.; Roy, P.; Birajdar, B. I.; Spiecker, E.; Schmuki, P. *Angew. Chem., Int. Ed.* **2009**, *48*, 9326. (b) Kim, Y. J.; Lee, M. H.; Kim, H. J.; Lim, G.; Choi, Y. S.; Park, N.-G.; Kim, K.; Lee, W. I. *Adv. Mater.* **2009**, *21*, 3668. (c) Chen, D.; Huang, F.; Cheng, Y.-B.; Caruso, R. A. *Adv. Mater.* **2009**, *21*, 2206. (d) Chen, D.; Cao, L.; Huang, F.; Imperia, P.; Cheng, Y.-B.; Caruso, R. A. *J. Am. Chem. Soc.* **2010**, *132*, 4438. (e) Brezesinski, T.; Wang, J.; Polleux, J.; Dunn, B.; Tolbert, S. H. *J. Am. Chem. Soc.* **2009**, *131*, 1802. (f) Liu, X.; Gao, Y.; Cao, C.; Luo, H.; Wang, W. *Langmuir* **2010**, *26*, 7671.

(14) (a) Ren, Y.; Hardwick, L. J.; Bruce, P. G. *Angew. Chem., Int. Ed.* **2010**, *49*, 2570. (b) Chen, J. S.; Tan, Y. L.; Li, C. M.; Cheah, Y. L.; Luan, D.; Madhavi, S.; Boey, F. Y. C.; Archer, L. A.; Lou, X. W. *J. Am. Chem. Soc.* **2010**, *132*, 6124. (c) Kim, S.-W.; Han, T. H.; Kim, J.; Gwon, H.; Moon, H.-S.; Kang, S.-W.; Kim, S. O.; Kang, K. *ACS Nano* **2009**, *3*, 1085. (d) Yue, W.; Randorn, C.; Attidekou, P. S.; Su, Z.; Irvine, J. T. S.; Zhou, W. *Adv. Funct. Mater.* **2009**, *19*, 2826.

(15) Jun, Y.-w.; Casula, M. F.; Sim, J.-H.; Kim, S. Y.; Cheon, J.; Alivisatos, A. P. *J. Am. Chem. Soc.* **2003**, *125*, 15981.

(16) (a) Zhang, Z.; Zhong, X.; Liu, S.; Li, D.; Han, M. *Angew. Chem., Int. Ed.* **2005**, *44*, 3466. (b) Jiang, D.; Xu, Y.; Hou, B.; Wu, D.; Sun, Y. *Eur. J. Inorg. Chem.* **2008**, 1236. (c) Tsai, M. T. *J. Non-Cryst. Solids* **2002**, *298*, 116.

(17) Liu, C.; Yang, S. *ACS Nano* **2009**, *3*, 1025.

(18) (a) Pinna, N.; Niederberger, M. *Angew. Chem., Int. Ed.* **2008**, *47*, 5292. (b) Mutin, P. H.; Vioux, A. *Chem. Mater.* **2009**, *21*, 582.

(19) (a) Nolan, N. T.; Seery, M. K.; Pillai, S. C. *J. Phys. Chem. C* **2009**, *113*, 16151. (b) Kang, C.; Jing, L.; Guo, T.; Cui, H.; Zhou, J.; Fu, H. *J. Phys. Chem. C* **2009**, *113*, 1006. (c) Ding, K.; Miao, Z.; Hu, B.; An, G.; Sun, Z.; Han, B.; Liu, Z. *Langmuir* **2010**, *26*, 10294.

(20) (a) Zhang, J.; Li, M.; Feng, Z.; Chen, J.; Li, C. *J. Phys. Chem. B* **2006**, *110*, 927. (b) Zhang, J.; Xu, Q.; Li, M.; Feng, Z.; Li, C. *J. Phys. Chem. C* **2009**, *113*, 1698.

(21) Zachau-Christiansen, B.; West, K.; Jacobsen, T.; Atlung, S. *Solid State Ionics* **1988**, *28*−*30*, 1176.

(22) (a) Lou, X. W.; Archer, L. A. *Adv. Mater.* **2008**, *20*, 1853. (b) Guo, Y.-G.; Hu, Y.-S.; Sigle, W.; Maier, J. *Adv. Mater.* **2007**, *19*, 2087.